**Author(s):** Akkanen, Suvi-Tuuli M.; Arias-Muñoz, Juan C.; Emelianov, Aleksei V.; Mentel, Kamila K.; Tammela, Juhani V.; Partanen, Mikko; Das, Susobhan; Faisal, Ahmed; Pettersson, Mika; Sun, Zhipei

**Title:** Enhanced Nonlinear Optical Responses in MoS2 via Femtosecond Laser-Induced Defect-Engineering

**Year:** 2024

**Version:** Published version

ADVANCED FUNCTIONAL MATERIALS
www.afm-journal.de

# Enhanced Nonlinear Optical Responses in $MoS_2$ via Femtosecond Laser-Induced Defect-Engineering

*Suvi-Tuuli M. Akkanen,* Juan C. Arias-Muñoz, Aleksei V. Emelianov, Kamila K. Mentel, Juhani V. Tammela, Mikko Partanen, Susobhan Das, Ahmed Faisal, Mika Pettersson, and Zhipei Sun**

**2D materials are a promising platform for applications in many fields as they possess a plethora of useful properties that can be further optimized by careful engineering, for example, by defect introduction. While reliable high-yield defect engineering methods are in demand, most current technologies are expensive, harsh, or non-deterministic. Optical modification methods offer a cost-effective and fast mechanism to engineer the properties of 2D materials at any step of the device fabrication process. In this paper, the nonlinear optical responses of mono-, bi-, and trilayer molybdenum disulfide ($MoS_2$) flakes are enhanced by deterministic defect-engineering with a femtosecond laser. A 50-fold enhancement in the third harmonic generation (THG) and a 3.3-fold increase in the second harmonic generation (SHG) in the optically modified areas is observed. The enhancement is attributed to resonant SHG and THG processes arising from optically introduced mid-band gap defect states. These results demonstrate a highly controllable, sub-micrometer resolution tool for enhancing the nonlinear optical responses in 2D materials, paving the way for prospective future applications in optoelectronics, quantum technologies, and energy solutions.**

## 1. Introduction

Two-dimensional (2D) materials have gained significant interest as a platform for the ever-shrinking devices in electronics and optoelectronics due to their efficient surface-to-volume ratio and unique chemical and physical properties.[1,2] Transition metal dichalcogenides (TMDs) are a notable subset of 2D materials, characterized by the chemical structure of $MX_2$ where $M$ is a transition metal and $X$ is a chalcogen atom. They exhibit, among other things, a layer-dependent bandgap,[3] versatile excitonic behavior,[1] and semiconductor, metallic, and superconductor phases.[3,4]

Among the most interesting traits of TMDs are their nonlinear optical (NLO) properties. TMDs have highly effective nonlinear susceptibilities and due to their atomic thickness phase-matching conditions can be relaxed.[5] This makes TMDs a great prospective platform for nonlinear optical applications. However, several challenges hinder the use of TMDs in NLO applications. In their most common crystalline form, 2H phase, even-layered group VI[6] TMD flakes have inversion symmetry, which prohibits the existence of even-order NLO phenomena, such as second harmonic generation (SHG). Additionally, the otherwise advantageous atomic thickness of 2D materials reduces the light-matter interactions to two dimensions, thus presenting conversion efficiency challenges for most NLO processes.

One method to enhance conversion efficiency is by enhancing the nonlinear response with defect engineering.[7,8] Defects in 2D materials have a much larger influence on the material properties compared to their bulk counterparts[9] and the introduction of defects has been shown to trigger many other intriguing effects such as phase change,[10] improved electrical properties,[7] and creation of quantum emitters.[11] However, typical defect introduction methods (e.g., plasma etching, thermal annealing, electron beam irradiation, and controlled chemical vapor deposition (CVD))[12] can be harsh and expensive. Additionally, most of these methods are not deterministic or can not be conducted after device fabrication without damaging the sample.

Optical modification methods present themselves as prospective pathways to rectify these issues.[13] These methods, namely laser modification, offer a fast and deterministic means for tuning 2D materials' properties post-fabrication cost-effectively with very few fabrication steps. The process utilized in this paper

S.-T. M. Akkanen, J. C. Arias-Muñoz, J. V. Tammela, M. Partanen, S. Das, A. Faisal, Z. Sun
Department of Electronics and Nanoengineering
Aalto University
Espoo 02150, Finland
E-mail: suvi-tuuli.akkanen@aalto.fi; zhipei.sun@aalto.fi
A. V. Emelianov, K. K. Mentel, M. Pettersson
Nanoscience Center
Department of Chemistry
University of Jyväskylä
Jyväskylä 40014, Finland

The ORCID identification number(s) for the author(s) of this article can be found under https://doi.org/10.1002/adfm.202406942



**DOI: 10.1002/adfm.202406942**

**Table 1.** Comparison of effectivity and ease of different $MoS_2$ SHG and THG enhancement methods.

| Enhancement method | SHG enhancement | THG enhancement | Fabrication steps | Deterministic |
|---|---|---|---|---|
| Plasmonic nanocavity Ref. [24] | 15-fold | 68-fold | 5 | No |
| Photonic crystal Ref. [25] | 170-fold | — | ⩾ 2 | No |
| Nanowire Ref. [26] | 12-fold | — | 2 | No |
| Defects Ref. [8] | 100-fold | — | 1 | No |
| Quantum dots Ref. [27] | 1500-fold | — | 5 | No |
| Periodic hyperbolic metamaterial Ref. [28] | 22145-fold | — | ⩾ 3 | No |
| Plasmonic stack structure Ref. [29] | — | 16-fold | ⩾ 4 | No |
| This work | 3.3-fold | 50-fold | 2 | Yes |

employs a femtosecond pulsed laser in an inert environment to induce local defects in 2D materials.[14–16] The method has previously been demonstrated in CVD-grown graphene resulting in up to 60 nm tall 3D structures of 2D material, luminescence,[17] and increased stiffness,[18] and in CVD molybdenum disulfide ($MoS_2$) resulting in defect-modified fluorescence timescale.[19] The present optical modification method is fast, cost-effective, highly reproducible, and easily tunable by changing laser parameters, such as power, spot size, wavelength, and irradiation time.

The focus of this paper is to study the effects of ultrafast optical modification on the nonlinear optical properties of mechanically exfoliated few-layer $MoS_2$. We find that the optical patterning significantly enhances both SHG and third harmonic generation (THG) in $MoS_2$, subsequently improving the conversion efficiency for both processes. The enhancement mechanism is attributed to the creation of mid-gap defect states that can resonantly enhance the nonlinear optical phenomena. The paper offers proof-of-concept for highly controllable, sub-micron resolution patterning of NLO enhanced areas on TMDs, which is essential for applications that require intricate structure design or precise spatial control, such as subwavelength light sources,[20] quantum computing[21] and hydrogen production[22] platforms, and nonlinear optical processors for neural networks.[23] The true advantage of this method lies in its deterministic nature and minimal fabrication steps as demonstrated in **Table 1** where different nonlinear enhancement methods are compared.

## 2. Results and Discussion

### 2.1. Optically Modified Structures in $MoS_2$

A femtosecond laser is used to pattern mono, bi, and trilayer $MoS_2$ flakes in a nitrogen gas atmosphere. For the purposes of this study, the optical characterization is focused on odd-layer flakes as even-layer $MoS_2$ flakes do not exhibit SHG,[30] however, some bilayer flakes are used for structural characterization and THG measurements.

The laser is used to expose three types of structures: single-point spots, lines, and squares. The lines and squares are created by overlapping single-point spots, as illustrated in **Figure 1a**. Different irradiation parameters, chosen based on previous studies[16–19,31] and tests, are used to determine the effect of varying exposure doses on the optical properties of $MoS_2$. The resulting optically modified areas of the $MoS_2$ flakes, presented in Figure 1b–d insets, are apparent in optical images as lighter, slightly green-tinted areas, indicating higher reflection, which is also confirmed by a reflection measurement. See Section S1 (Supporting Information) for testing and selection of the optical modification parameters for flakes and the reflection measurement results.

The topography of the optically modified areas is characterized by atomic force microscopy (AFM). The heights of the odd-layer flakes and their modified areas (Figure 1b–d) are obtained by fitting a Boltzmann function to cross-sectional AFM height profiles. The AFM scans and Boltzmann fits are presented in Figure S3 (Supporting Information) for the monolayer (1L) and Figure S4 (Supporting Information) for the trilayer (3L) flakes. The measured thicknesses of both pristine 1L (≈9 nm) and 3L (≈7 nm) flakes differ from typical 1L (≈0.65 nm)[32] and 3L (≈2 nm) flake thicknesses significantly but based on the linear and nonlinear optical characterization detailed later in this paper, the flakes are identified as 1 and 3L. This discrepancy is likely due to uneven contact between the flakes and the substrate, and residues from the transfer process of the flakes.[33] Based on the AFM scans, the optical modification increases the height of the flake for both 1L (highest growth ≈20 nm) and 3L (≈21 nm) flakes. However, the patterning does not affect the height of the substrate outside the flake, which suggests two possible scenarios for the height increase: either the process introduces strain to the modified areas[14] implying that they are suspended from the substrate, or there is a laser-assisted nanometric accumulation of material between(/on) the transferred flake and the substrate. To gain more understanding on this, nanoindentation measurements and strain simulations are performed. According to the simulation, the strain of the structures should be concentrated on their edges, which does not support the first hypothesis. Additionally, the indentation depth at the optically modified areas is much smaller than previous reports for suspended $MoS_2$[34] and the height of the structures does not change in the nanoindentation measurements, indicating the rigid character of the fabricated structures. See more details and discussion in Section S2.1 (Supporting Information) for nanoindentation and Section S6.1 (Supporting Information) for strain.

To understand the structures of the optically modified areas and the height increase, cross-sectional high-resolution transmission electron microscopy (TEM) and energy dispersive X-ray (EDX) analyses are conducted on an optically modified bilayer (2L) flake. Optical modification parameters and characterization results for the 2L flake are presented in Figure S5 (Supporting Information). **Figure 2a** shows a low-magnification cross-sectional

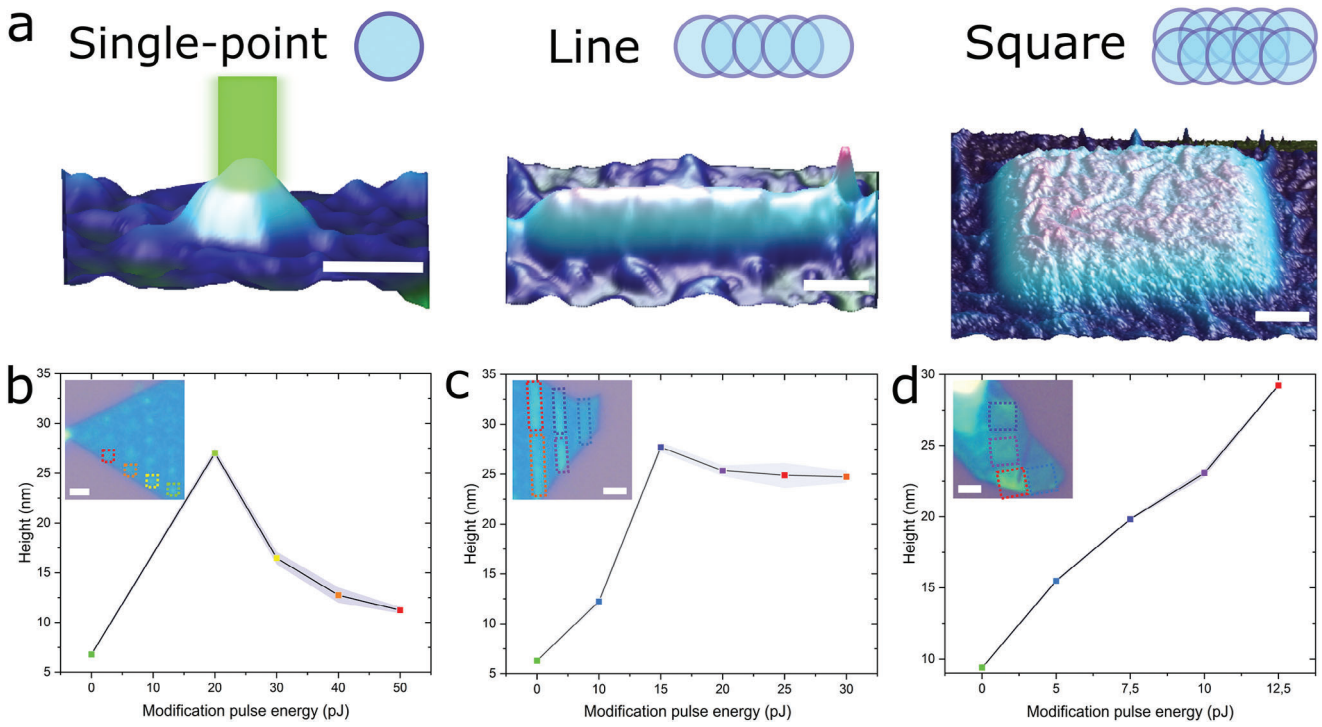


**Figure 1.** 3D AFM maps and height profiles of optically modified single-point spots and structures created by overlapping them. a) 3D AFM maps of single-point, line, and square structures and illustrations of their formation by overlapping single-points. The scale bar of the AFM maps is 0.5 µm, b) height profiles of four single-point spots in a 3L flake as a function of the used modification pulse energy, c) height profiles of the modified lines in a 3L flake as a function of the used modification pulse energy, and d) height profiles of the modified squares in a 1L flake as a function of the used modification pulse energy. Optical images of the single-points, lines, and squares are shown in the insets. The scale bar of the optical images is 2 µm and the color of the dashed rectangles corresponds to a modification pulse energy in each graph respectively (e.g., red dashed rectangle in b) = 50 pJ, c) = 25pJ, and d) = 12.5 pJ).

TEM micrograph of an edge of an optically modified square created with a modification pulse energy of 15 pJ. There are five distinct layers in the micrograph, listed here in ascending order: silicon dioxide substrate, a light-colored unknown layer on both sides of a thin dark line, which is the $MoS_2$ flake, a thick black layer from evaporated platinum, and grainy gray layer from sputtered platinum. Both platinum layers were deposited to protect the optically modified structure from damage during the ion-beam preparation of the lamella (see methods for more details).

The optically modified structure is readily identifiable as the dark, thin line ($MoS_2$) diminishes toward the right side of the image, while the light-colored layers surrounding it widen. Upon examining a higher magnification image of the pristine 2L flake (Figure 2b) and a Fast Fourier Transform (FFT) (Figure 2c), it is evident that the flake is initially crystalline and its thickness (≈1.44 nm) aligns with the theoretical 2L $MoS_2$ thickness (≈1.2-1.7 nm[32,35]). Also visible here are the faint light-colored layers on both sides of the pristine flake. These layers, likely caused by polymer residues from the transfer process, exhibit thicknesses of ≈2.2 nm below and ≈1.5 nm above the flake. Indeed, the total height of the 2L $MoS_2$ flake and the light-colored layers (≈5.2 nm), as determined from the TEM results, closely matches the height measured by AFM (≈5.5 nm), explaining the previous height discrepancies of the 1 and 3L flakes.

When the edge of the patterned area is examined more closely (Figure 2d), an abrupt change in the structure of the $MoS_2$ is observed as it becomes indistinct (Figure 2e). This suggests degradation of the crystal structure, likely due to the introduction of defects and stretching of the chemical bonds at the edges of the elevated structures. Simultaneously, the light-colored layers around the flake start to grow. After moving from the edge to the more flat center of the modified area, the structure regains crystallinity (Figure 2f) and a thickness consistent with that of the pristine flake. Interestingly, here the light-colored layers have significantly thickened to ≈12.9 nm below and ≈7.9 nm above the flake. This supports the second of the previously proposed hypotheses: optical modification triggers a foreign material accumulation process in the laser-exposed regions of $MoS_2$.

A closer examination of the foreign material through a FFT analysis (Figure 2g) reveals no evidence of crystallinity, indicating that the material is likely amorphous or gaseous, although there are several reasons why the material is more likely an amorphous solid. Namely, the 3D structures remained rigorous through high vacuum and cryogenic and nanoindentation measurements.

As the evidence supports the foreign material being amorphous and solid, its chemical composition can be analyzed via EDX. Figure 2h displays the atomic weight percentages of the different elements, carbon, oxygen, copper (from the TEM grid, can be excluded), silicon, molybdenum, and sulfur, detected from four different measurement areas (substrate, flake, and light-colored layers below and above the $MoS_2$ flake). From these results, it can be concluded that the accumulated foreign material is

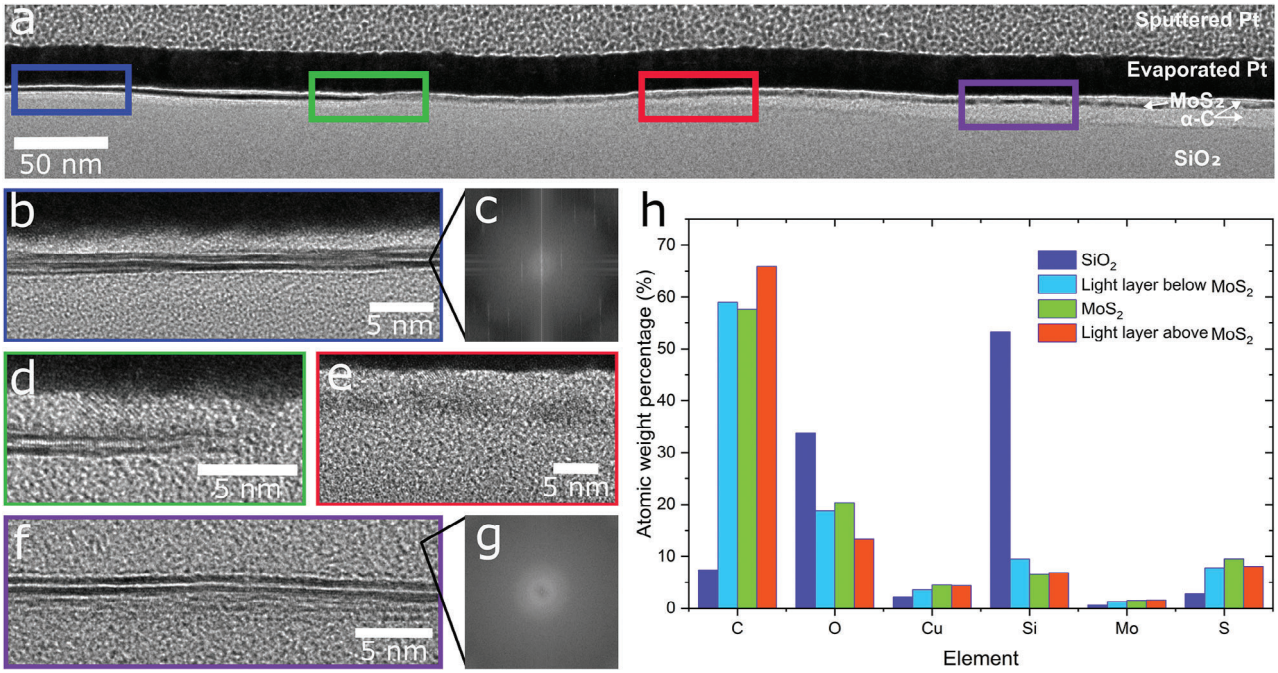


**Figure 2.** TEM micrographs and EDX analysis of the optically modified areas in a 2L $MoS_2$ flake. a) Low magnification TEM image of pristine (left side) and optically modified (right side) area of the flake. Colorful squares indicate the positions of higher magnification images in b, d, e, and f. b) high-magnification TEM image of a pristine 2L $MoS_2$ structure, c) a FFT analysis of the pristine 2L flake crystallinity, d) high-magnification TEM image of the interface between pristine and modified regions of the flake, e) high-magnification TEM image of the $MoS_2$ structure on the edge of the optically modified region, f) high-magnification TEM image of pristine-like $MoS_2$ structure on the central part of a modified region, g) a FFT analysis of the crystallinity of the light-colored layers (carbon) around the $MoS_2$ structure in f), and h) EDX analysis of the different layers of the TEM sample in a). The copper signal is from the TEM grid.

most likely amorphous carbon ($\alpha$-C). Neither the molecular ratios nor the FFT analysis indicate that the accumulated carbon has a crystalline structure, ruling out graphite, other carbon allotropes, as well as silicon carbide. More evidence and discussion on the detected elements and possible sources of carbon are presented in Section 3 (Supporting Information).

Probing the vibrational and excitonic properties of 2D materials can offer more detailed information on the changes in crystal and band structure than many physical characterization methods. To this end, the optically modified $MoS_2$ structures are characterized by Raman, low-frequency (LF) Raman, and PL spectroscopies. The intrinsic Raman active vibrational modes, $E^1_{2g}$ ($\approx$385.5 $cm^{-1}$ for 1L squares, $\approx$383.3 $cm^{-1}$ for 3L lines) and $A_{1g}$ ($\approx$404,3 $cm^{-1}$ for 1L squares, $\approx$406.7 $cm^{-1}$ for 3L lines), presented in **Figure 3**a for 1L and 3b for 3L flake, show a decrease in intensity upon optical modification, indicating damage to the crystal structure. Significant damage could lead to ablation of the layers but as the layer-characteristic peaks of the LF Raman spectra (Figure S8, Supporting Information) remain intact, this is not the case here.

While decreasing Raman intensity can indicate damage, shifting of the Raman peaks can provide valuable information on the type of damage, namely defects. When considering high-energy laser irradiation, the most relevant defect types are chalcogen vacancies,[36] substitutional atoms, anti-site/interstitial atoms,[12] and strain.[37] The Raman peaks have been shown to shift differently depending on the defect concentration and type. For example, chalcogen vacancies have been demonstrated to induce considerable $E^1_{2g}$ redshift and negligible $A_{1g}$ blueshift.[38] Strain creates a similar $E^1_{2g}$ redshift but has also been shown to cause splitting of the peak, setting it apart from vacancies.[39] Different doping defects, including substitutional defects, also behave distinctly differently from vacancies, showing mostly shifting in the $A_{1g}$ mode[39] and depending on doping concentration, brand new peaks (e.g., from oxidation or chalcogen exchange).[40]

There is no significant shifting or broadening of the Raman peaks detected on the optically modified areas of the 1 and 3L flakes. However, while no peak shifts are detected in the squares and lines patterned with relatively gentle optical modification parameters, a small $E^1_{2g}$ peak redshift ($\approx$0.76 $cm^{-1}$) is observed when harsher parameters (60 pJ pulse energy, 5 s irradiation time) are used to pattern a single-point spot on the 3L flake (Figure S9, Supporting Information). This indicates that the defect introduction process is not substitution atoms or doping-related. Further, no signal from possible substitutional atoms, namely oxygen and carbon, is detected (see wide-range Raman spectra in Figure S10, Supporting Information). Interestingly, there is an increase in the PL intensity of the samples after 12 months (See Figure S12, Supporting Information). This could indicate that over time, the optically modified areas can self-heal and fill the chalcogen vacancies with oxygen atoms. However, there is no indication that oxidation is behind the initial changes in the linear and nonlinear responses. See more discussion on performance over time and durability in Section S5 (Supporting Information):

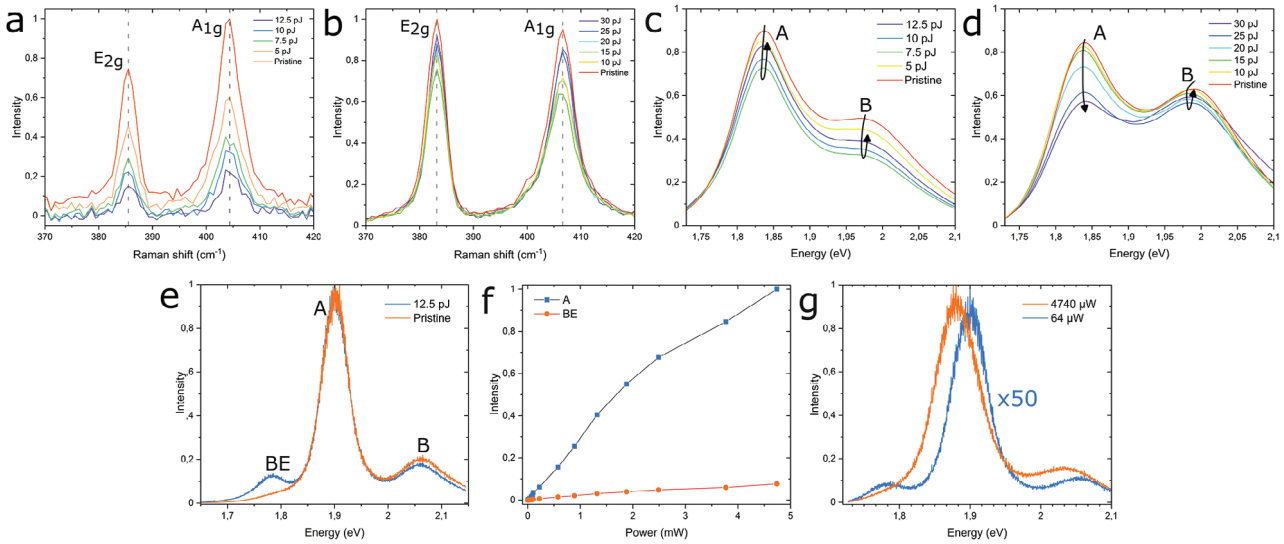


**Figure 3.** Raman and PL spectra of the 1L and 3L flakes and low-temperature PL measurements of optically modified areas. a) Raman spectra of the optically modified squares in the 1L flake in contrast to the pristine area, b) Raman spectra of the optically modified lines in the 3L flake in contrast to the pristine area, c) smoothed room-temperature PL spectra of the optically modified squares in the 1L flake, d) smoothed room-temperature PL spectra of the optically modified lines in the 3L flake, e) low-temperature (80 K) PL spectra of the highest modification pulse energy square and pristine 1L flake. The incident power for the PL measurement is 800 μW. f) Low-temperature A exciton and BE PL peak intensities of an optically modified square as a function of PL excitation power, and g) low-temperature high and low excitation power PL spectra of an optically modified 1L flake square. The optical modification pulse energy for the square in (e,f) is 12.5 pJ.

Durability. Similarly for carbon, although faint amorphous carbon peaks are detected for the highest modification pulse energies, significant effects from carbon substitutional atoms can be ruled out as they have been shown to induce $A_1g$ peak shifts and major changes to band structure,[41] which were not detected in the PL measurements detailed next.

Mirroring the trends seen in the Raman spectra, the PL spectra of the flakes also decrease in intensity upon optical modification as seen for both 1 and 3L flakes in Figure 3c,d, respectively. However, the reduction is much less pronounced than the Raman intensity decrease (20% vs 70%), and it does not follow the same pattern for the 1L flake. Here, the square with 7.5 pJ modification pulse energy has the lowest PL instead of the highest modification pulse energy pattern (12.5 pJ), although the differences between the intensities of the irradiated areas are minor. Similarly to Raman, there is no significant shifting in the position of either the A or B exciton for either 1L or 3L flake, but there is a change in the ratio of the exciton contributions for the 3L flake as the A exciton's intensity decreases more and eventually drops below the B exciton's intensity for the 30 pJ modification pulse energy pattern. Additionally, the B exciton exhibits some broadening with the harshest modification parameters. PL maps of the flakes are presented in Figure S11 (Supporting Information).

The lack of PL shifting further confirms that the optical modification does not induce strain[42] or add-atoms[43] on the structures but could introduce vacancy defects. While defect-introduced states can cause shifting of the PL due to decreased trion ($X^-$) contribution[44] or even emergence of a new bound exciton (BE) peak at 1.75 eV,[44,45] these effects can be very subtle at room temperature, especially for low defect concentrations.[45] However, these changes can readily be probed in low-temperature measurements.

Indeed, a new PL peak emerges near 1.78 eV (≈697 nm) in the optically modified areas measured in low-temperature (80 K)(Figure 3e). The emerging BE peak has a similar intensity to the B exciton and a relatively narrow width (≈0.067 eV/26 nm), which indicates that the defect states are located in the same general area of the band gap but are spread over varying energy levels.[46] The behavior of the BE peak is further studied with power-dependent low-temperature PL measurements. The intensities of A and BE peaks as a function of excitation power are presented in Figure 3f (spectra in Figure S11, Supporting Information) and a comparison of one low (64 μW) and one high (4740 μW) excitation power spectra in Figure 3g. The BE peak is discernible in the low power measurements but due to the red-shifting and broadening of the A peak, most likely due to laser-induced heating, it becomes hard to distinguish with higher excitation energies. The intensity of the BE peak has a much weaker relation to increasing excitation energies than the A peak and the intensity shows signs of saturating with higher energies, although the saturation point is not reached as increasing excitation energies could lead to damaging the sample or local heating effects that could further complicate understanding the results. Previously stagnation of the PL intensity has been attributed to the saturation of the defect states of the bound excitons,[47] supporting the hypothesis that optical modification introduces chalcogen vacancies.

### 2.2. Nonlinear Optical Measurements

It has been shown that the nonlinear optical properties of TMDs can be enhanced through defect engineering.[8] To study this, the SHG of the optically modified areas is measured with a

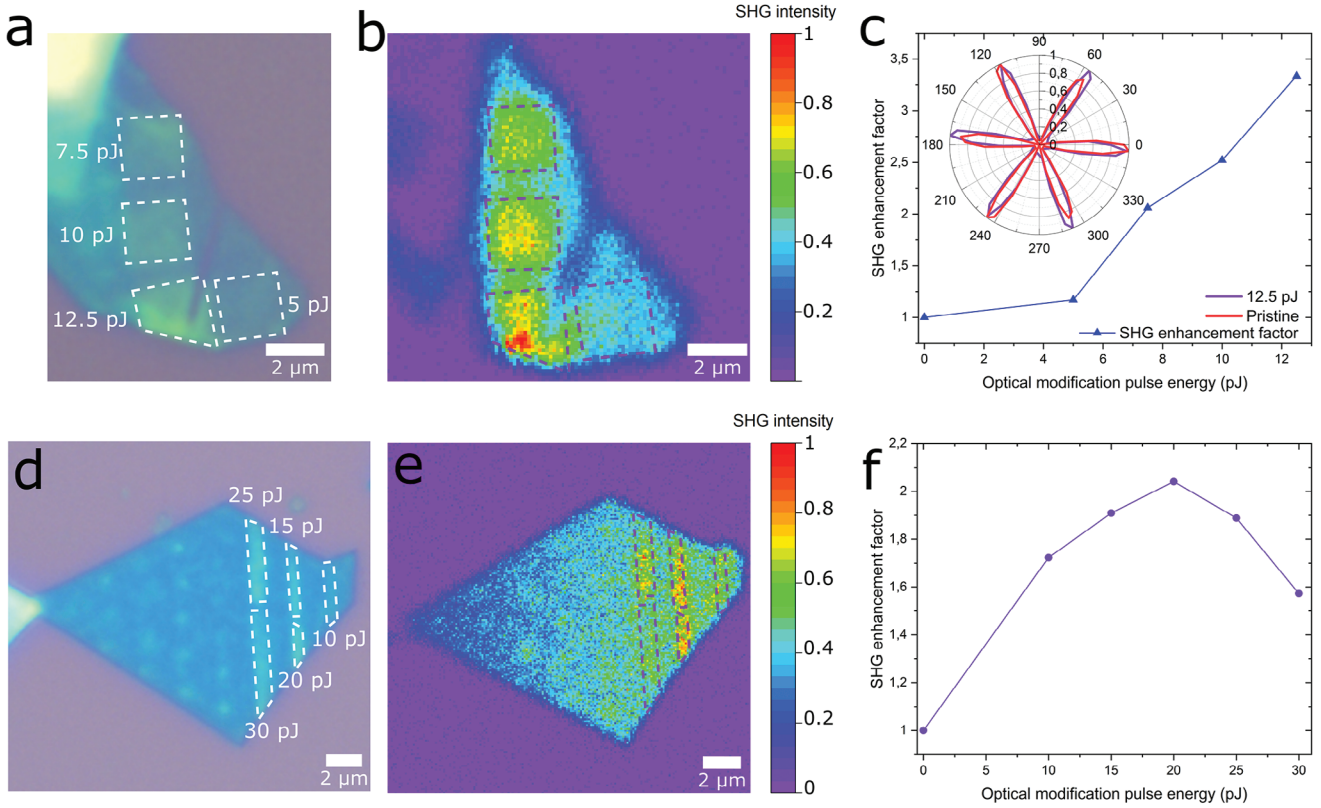


**Figure 4.** Polarization, wavelength, and optical modification pulse energy dependent SHG measurements. a) Optical image and patterning parameters of the 1L flake, b) SHG map of the 1L flake, c) optical modification pulse energy dependent SHG enhancement for the 1L flake. Polarization-dependent SHG for pristine and 12.5 pJ modification pulse energy in inset. d) Optical image and patterning parameters of the 3L flake line patterns, e) SHG map of the 3L flake, and f) optical modification pulse energy dependent SHG enhancement for the 3L flake line patterns. The white and purple dashed areas in optical images and SHG maps mark the optically modified square and line areas.

mapping setup (see methods section for details) using a fundamental wavelength $\lambda_f$ of 800 nm ($\lambda_{SHG}$ = 400 nm).

An optical microscope image of the 1L flake with the optical modification parameters is displayed with the measured SHG map in **Figure** 4a,b, respectively. The modified areas, aside from the 5 pJ modification pulse energy square, are clearly distinguishable from the SHG map as they exhibit higher second harmonic response than the pristine flake, reaching a ≈3.3-fold enhancement factor (Figure 4c) at the highest modification pulse energy square (12.5 pJ). The variance of the enhancement factor in the area is 0.14 (≈4 %), indicating that the modification is quite uniform in the whole structure.

Additionally, the SHG intensity dependence on the polarization of the incident light for both the pristine 1L flake and the highest modification pulse energy square is shown in the inset of Figure 4c. Both polarization plots exhibit the typical six-fold symmetry of $MoS_2$, however, there are variations in the intensity of the folds of the modified area polarization plot. Changes in polarization dependence can offer insight into the types of defects present; for example, the strain has been seen to alter the polarization-dependent symmetry.[48,49] While strain has been excluded as the mechanism behind the observed changes in this paper, the optical modification could relieve some of the tension created by the transfer process in the flat part of the flakes, leading to minor alterations in polarization dependence. It is more likely that these alterations are the result of the amorphous carbon accumulated below and on the flake. The polarization-dependent SHG intensity plots for all the modified areas in the 1L flake are provided in Figure S13 (Supporting Information).

An optical image of the 3L flake with optical modification parameters and a 3L flake SHG map are presented in Figure 4d,e, respectively. Here, the analysis is focused on the optically modified line structures as the single-point spots are too small to extract reliable results. As in the 1L flake, the optically modified areas exhibit enhanced SHG. Contrary to the 1L flake, here the highest enhancement factor (Figure 4f), ≈2-fold with a standard deviation of 0.24 (≈11 %), is obtained for a 20 pJ modification pulse energy pattern instead of the highest used pulse energy (30 pJ) pattern. This indicates that there is a threshold for beneficial defect concentration for NLO applications, after which the introduction of defects becomes detrimental. Indeed, a SHG reduction has previously been reported for optically modified areas on CVD $MoS_2$ patterned with a 60 pJ pulse energy,[19] reinforcing this notion.

To better elucidate a connection between the nonlinear enhancement and the defects, the defects are quantified by determining the estimated interdefect distances from intensity ratios[50] of defect-related Raman peaks and characteristic Raman peaks (Section S1, Supporting Information). The results indicate that an optimal defect distance for SHG enhancement is

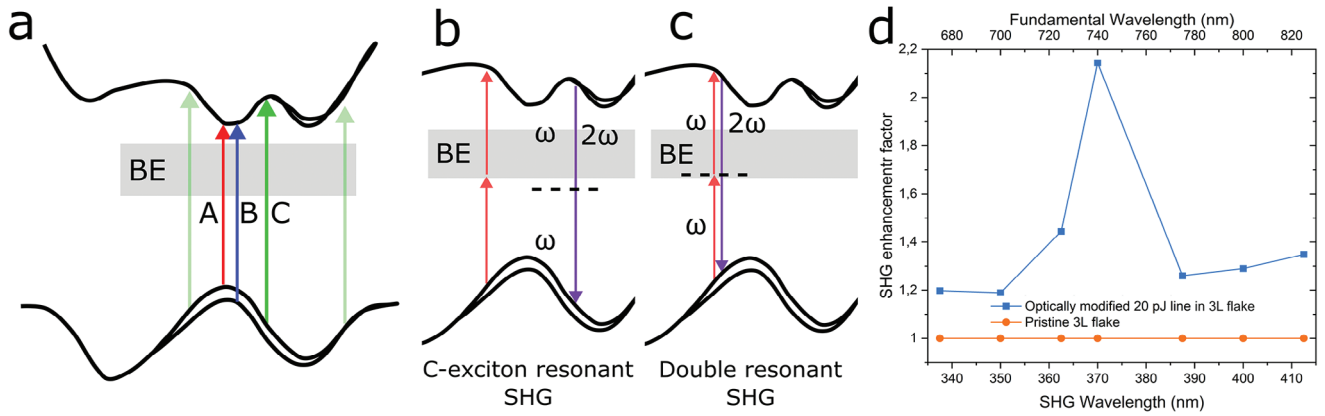


**Figure 5.** Schematic representation of $MoS_2$ band gap, resonant SHG processes, and wavelength-dependent SHG measurements. a) Schematic representation of 1L $MoS_2$ band gap. A, B, and C note the exciton transitions, and BE the level of the bound excitons. The band structure is based on a DFT simulation performed with Quantum Espresso, b) C-exciton resonant SHG process, c) double resonant SHG process, and d) pump wavelength (/SHG wavelength) dependent SHG enhancement factors for pristine and optically modified area in the 3L flake.

≈3.5 nm, as this value corresponds to the highest SHG enhancement areas for both 1L (12.5 pJ) and 3L (20 pJ) samples.

The surface second-order nonlinear susceptibilities of the 1 and 3L flakes and their optically modified areas $\chi_s^{(2)}$ can be estimated by[51]:

$$\chi_s^{(2)} = \sqrt{\frac{\epsilon_0 c \lambda_{SHG}^4 P_{SHG} R \tau_f^2 (n_{SHG}+1)^2 (n_f+1)^4}{32 NA^2 \tau_{SHG} P_f^2 \phi}} \quad (1)$$

where $\epsilon_0$ is the vacuum permittivity, $c$ is the speed of light, $P_f$ and $P_{SHG}$ are the average powers for fundamental and SHG beams, $R$ is the repetition rate of the laser, $\tau_f = \tau_{SHG}$ are the fundamental and SHG pulse durations, $n_f = 1.4533$[52] and $n_{SHG} = 1.4701$[52] are the substrate refractive indices for fundamental and SHG wavelengths, and $NA$ is the numerical aperture of the objective. The $\phi$ term (≈3.56) comes from using Green's function in formulating this equation.[51]

The average powers of the SHG beams can be determined from the detector counts by relating the acquired signal level to the detected SHG power and applying relevant correction factors. This process is explained in detail in the methods section.

With the obtained powers, a $\chi_s^{(2)}$ value of $\approx 1.13 \times 10^{-21}$ m$^2$ V$^{-1}$ for pristine 1L $MoS_2$ and of $\approx 2.06 \times 10^{-21}$ m$^2$ V$^{-1}$ for the highest optical modification pulse energy (12.5 pJ) are calculated. Similarly for 3L flake, a $\chi_s^{(2)}$ of $\approx 2.63 \times 10^{-21}$ m$^2$ V$^{-1}$ for pristine and $\approx 4.01 \times 10^{-21}$ m$^2$ V$^{-1}$ for optically modified 20 pJ pulse energy line can be obtained.

From these values, the effective second-order nonlinear susceptibilities ($\chi_{eff}^{(2)}$) can be determined by dividing $\chi_s^{(2)}$ by the thickness of a typical monolayer (0.65 nm)[32] or trilayer (≈2 nm) $MoS_2$. This yields ≈3.16 and ≈2.01 pmV$^{-1}$ for the modified areas of the 1 and 3L flakes respectively, and ≈1.65 and ≈1.32 pmV$^{-1}$ for the pristine 1 and 3L flakes. The $\chi_s^{(2)}$ and $\chi_{eff}^{(2)}$ values for all optically modified areas for both of the flakes are listed in Section S6 (Supporting Information). The effective susceptibilities are in the same order of magnitude as in earlier reports for pristine $MoS_2$,[5,53] and there is a clear enhancement in the optically modified areas. Importantly, the conversion efficiency, which is one of the main obstacles with NLO applications of TMDs, is significantly improved. The conversion efficiency can be obtained by dividing the power of the resulting SHG by the power of the fundamental and we obtain a ≈233% increase for the highest enhancement area in 1L flake and ≈132% for the 3L flake, respectively.

There are several ways to enhance the SHG intensity, including using a wavelength that is resonant with a band structure feature i.e., matching the energy of the $\lambda_{SHG}$ photons with the exciton transition energies of $MoS_2$ (see **Figure 5**a,b). It has also been shown that the introduction of chalcogen vacancy defects can enhance the SHG in TMDs[54–56] by creating states (BE) within the bandgap of the material that can also act as resonant states in the SHG process.[57] If this defect state resonance occurs simultaneously with the resonance with one of the exciton transitions, creating a double resonance, a significant enhancement can be obtained (Figure 5c). It should be noted, that the defect states are referred here as BE for convenience even though the bound excitons at the defect states can only exist in lower temperatures.

In order to confirm that the SHG enhancement detected in the optically modified structures is due to resonances with mid-gap defect states, wavelength-dependent SHG measurements are performed with pump wavelengths ranging from 600 nm ($\lambda_{SHG}$ = 300 nm) to 900 nm($\lambda_{SHG}$ = 450 nm). The resulting wavelength-dependent SHG enhancements are presented in Figure 5d, where the data is normalized by dividing both the pristine and optically modified area SHG signals of certain wavelength by the pristine (hence, pristine is a straight line). It should be noted that a wider range of measurements was performed but some wavelengths (>825 nm, <675 nm) did not produce any SHG signal, most likely due to limitations in our measurement setup, and are thus left out of the plot. As expected, a higher SHG enhancement factor is obtained for fundamental wavelengths between 700 nm (SHG 350 nm) and 775 nm (≈388 nm). The observed wavelength range is slightly different from the BE peak in the low-temperature PL measurements (≈684–709 nm), which can be explained by the temperature-dependent shifting and broadening of the energy state ranges. Based on the shifting and width

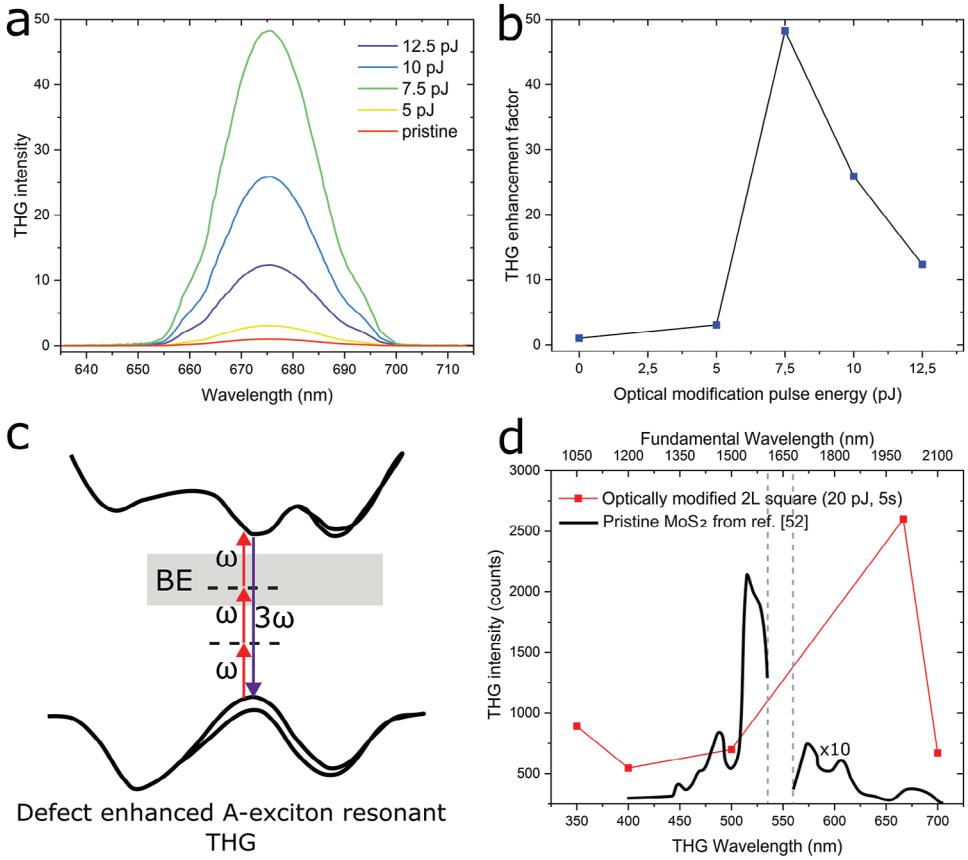


**Figure 6.** THG enhancement and wavelength-dependent THG enhancement. a) THG intensity spectra for all optically modified patterns in the 1L flake, b) THG enhancement factor as a function of the optical modification pulse energy, c) a schematic of resonant THG enhancement, and d) wavelength-dependent THG in an optically modified 2L square compared to pristine $MoS_2$ from Ref. [60].

changes of the A exciton peak from room temperature PL measurements (≈674 nm, FWHM = ≈40 nm) to 80 K (≈652 nm, FWHM = ≈20 nm), the BE states are similarly shifted and broadened to ≈717 nm and FWHM of ≈50 nm at room temperature, which corresponds quite well with the wavelength-dependent SHG measurements. The observed enhancement with 800 nm fundamental wavelength can be explained by overlapping of the BE and C exciton states, which increases the probability of the SHG process. Other changes in the measurements can also be explained by the fact that while some wavelengths may be resonant with the defect states, they may not resonate with the conduction band and the limitations and resolution of the measurement setup.

To avoid overlooking other enhancement mechanisms, different defect types and the accumulated amorphous carbon need to be considered. Doping/substitution from oxygen atoms has been shown to diminish the SHG response from $MoS_2$,[58] further strengthening the earlier conclusions from Raman and PL to exclude them as the defect type. The effect of the accumulation of amorphous carbon is less clear as it has been shown that thin layers of amorphous carbon can increase the reflectivity of $SiO_2$,[59] which could, in turn, enhance the SHG. However, according to our simulations (see Section S7.2, Supporting Information), the accumulation of amorphous carbon decreases the SHG due to reduced electric field amplitude, and thus can not be behind the observed enhancement here. In fact, the accumulation of carbon may be counteracting the nonlinear enhancement, necessitating an exploration and removal of the carbon source in the patterning process to mitigate this effect.

To probe the nonlinear enhancement further, THG measurements are concluded with a pump-probe setup using a fundamental wavelength of 2 µm, chosen for close resonance with the A exciton. More details about the setup can be found in the measurement section. The THG spectra of the modified areas in the 1L flake are presented in **Figure** 6a and the THG enhancement factor as a function of modification pulse energy in Figure 6b. The results show that the THG signal is enhanced in all optically modified areas of the 1L flake with a significant 50-fold enhancement of the THG intensity in the 7.5 pJ modification pulse energy square. Notably, the THG enhancement behaves differently from SHG, which had the highest enhancement with the highest modification pulse energy. This would indicate that the different modification pulse energies may introduce defects at distinctly different energy levels that can be more suitable for different nonlinear phenomena.

As with SHG enhancement, the THG enhancement mechanism is likely due to the mid-gap states and resonant effects in the THG process. Due to the limited range of the defect states, it is impossible to match all of the virtual states in the process with the defect states to gain total resonance as with SHG, but it is

certainly possible to still enhance THG as illustrated in Figure 6c. To confirm this, wavelength-dependent THG measurements are performed. Due to limitations of the measurement setup (THG signal in the deep UV), a resonance with all of the virtual states can not be probed. Nevertheless, the wavelength-dependent THG measurements exhibit enhancement for wavelengths between 550–700 nm. Remarkably, the observed enhancement (Figure 6d) is vastly different from the THG wavelength dependence exhibited by pristine $MoS_2$.[60] In the case of the pristine flake, the highest THG signal is achieved with wavelengths of 500–525 nm, beyond which the signal markedly significantly diminishes (by tenfold).[60] However, our findings indicate the opposite behavior where the THG intensity improves with higher THG wavelengths, implying the involvement of new resonant states.

## 3. Conclusion

In this paper, a controllable post-fabrication defect engineering method resulting in a ≈3.3-fold SHG enhancement, a ≈50-fold THG enhancement, and significant improvement of conversion efficiencies of both in mono and few-layer $MoS_2$ flakes is demonstrated. The enhancement is attributed to optically induced defects, that act as "real virtual" states in the nonlinear processes, enhancing their intensities via resonance. The existence of defects is confirmed by the emergence of a bound exciton peak in the low-temperature PL measurements, and wavelength-dependent SHG and THG measurements. The TEM measurements confirm that the crystalline structure remains mostly intact in the optically modified areas, hinting at a low concentration of defects, which is supported by our defect density estimations. We also find that the mechanism behind the optically induced 3D structures in 2D materials is an accumulation of amorphous carbon under and around the irradiated areas and possible strain on the edges of the structures. Replicable and deterministic defect engineering is a versatile tool for modifying 2D materials.[12] The method proposed and characterized here shows promise as a fabrication method for devices in quantum light sources,[61] laser and light modulation technologies,[5] optical neural networks,[62,63] and energy solutions[64–66] and seems especially promising for hydrogen evolution reaction, as both $MoS_2$ - carbon heterostructures[64,65] (like our amorphous carbon 3D structures) and TMD defects[66] (as demonstrated here) have been shown to act as a catalyst in the reaction, enabling more efficient energy solution devices.

## 4. Experimental Section

*Sample Fabrication*: The $MoS_2$ flakes were exfoliated with the scotch-tape method from the bulk crystal (2D semiconductors) using first Nitto tape and then polymethylsiloxane (PDMS). Suitable flakes were identified with optical microscopy and dry-transferred on a 285 nm $SiO_2$ on Si substrate with a deterministic transfer system. Samples were cleaned with acetone and isopropyl alcohol. The laser patterning of the samples was carried out in a nitrogen gas environment with Pharos-10, Light Conversion Ltd. femtosecond laser (515 nm, 600 kHz, 250 fs). The full details of the laser patterning setup can be found in the reference[67] and details of laser parameters in Figure S1 (Supporting Information).

*AFM*: The topography of the flakes was investigated with an atomic force microscope (Bruker, Dimension Icon) using Scan–Asyst Air tips and operation mode (tapping mode). The nanoindentation measurements were concluded with RTESPA-150 tip and PeakForce quantitative nanoscale mechanical mapping mode with the relative method.

*Raman, Low-Frequency Raman and PL Spectroscopy*: The Raman and PL analyses of the samples were conducted with a WITec alpha300 RA+ Micro-Raman setup that utilizes a confocal microscope in a backscattering configuration. The excitation wavelength was 532 nm (Nd:YAG solid-state laser), spectrometer (Newton Andor EMCCD) grating was 1800 $mm^{-1}$ (Raman) and 600 $mm^{-1}$ (PL). The spectra and maps were collected using a 100X CF Plan Nikon objective (NA = 0.95). The laser power used for the measurements was 800 μW. The low-frequency modes were collected using the Rayshield mode of the device. The low-temperature PL measurements were conducted with a Zeiss 50x objective with a numerical aperture of 0.55 in a liquid nitrogen-cooled LinkAm stage.

*Cross-Sectional HR-TEM and EDX Analysis*: In preparation for TEM and EDX, a lamella of the sample was prepared by an Argon ion-milling technique in a JEOL JIB-4700F multibeam system. The sample was first protected with platinum (20 nm via metal evaporation (Angstrom engineering), 2 μm sputtering in the multibeam system), then milled with ions and attached to a micromanipulator that moved the lamella to a TEM grid. The HR-TEM and EDX were conducted on a bilayer sample with a JEOL JEM-2200FS Field emission microscope. The HR-TEM has a resolution of 0.7 Å and the EDX has a spatial resolution of <1 nm.

*SHG Measurements*: The high-resolution mapping was conducted on a homebuilt multiphoton mapping setup. The samples were pumped with ≈0.6 mW power and 800 nm wavelength with Pharos–Orpheus, Light conversion Ldt, femtosecond laser (752 kHz, 120 fs), and the micrographs were obtained by scanning with a galvanometric scanner through Nikon Plan N 40x (NA = 0.75) objective in a reflection configuration. The nonlinear response was measured with a Hamamatsu 7844 photomultiplier tube (PMT) after filtering out the fundamental wavelength with a 550 nm long-pass (LP) dichroic mirror and a 400 nm band-pass(BP) filter.

The polarization measurements were conducted with the same parameters as the high-resolution maps and the polarization dependence was obtained by rotating a half-wave plate whilst using a linear polarizer to select the parallel polarization component from the generated harmonic optical field. Full details on a similar experimental setup can be found in Ref. [68].

The wavelength-dependent SHG measurements were conducted with the same setup by changing the pump wavelength and the filters before the PMT as detailed in Table S1 (Supporting Information).

The SHG powers used in the second order nonlinear susceptibility calculations were determined by relating the measured PMT counts to SHG power. To obtain such conversion value, several steps must be followed: First, the voltage of the data acquisition (DAQ) unit is related to the count by scaling the count value with the DAQ sampling rate and the integration time. This ratio (counts/V) can be used to determine the DAQ voltage for any number of counts. Then any correctional factors from equipment between the DAQ and PMT must be considered. The PMT has gain and a certain cathode sensitivity to wavelength that both affect the values determined by the unit. For the PMT, the cathode sensitivity at 400 nm ($\lambda_{SHG}$) is ≈ 76 mA $W^{-1}$ and the gain at 0.6 V control voltage is ≈$2 \times 10^5$. When the sensitivity is multiplied by the control voltage, the value (A/W) that goes to the amplifier unit is obtained. The amplifier has a certain transimpedance (≈$10^7$ V $A^{-1}$) and when multiplied with the earlier value, results in a V/W value which can then directly be compared to the counts/V value determined in the beginning to obtain the power. This method yields the power of the SHG at the PMT and does not account for losses from the optics, so the real $P_{SHG}$ is likely higher by at least several percent.

*THG Measurements*: The third harmonic generation measurements were conducted on two different homebuilt pump-probe setups. The THG from the 1L sample was measured with a TOPAS, Light conversion Ldt, (2 μm, 2 kHz, 200 fs) pump laser aligned through Nikon 40x (NA = 0.75) objective to the sample and the generated THG signal was collected by a monochromator with a photomultiplier detector. The fundamental beam was filtered out by 800 nm and 1300 nm short-pass filters.

The wavelength-dependent THG measurements were conducted with an ultrafast femtosecond laser (Pharos–Orpheus, Light conversion Ldt,) at 752 kHz repetition rate, with a pulse duration of 120 fs. The light was

focused with a Thorlabs 40x reflective objective (NA = 0.5), filtered through an 800 short-pass filter, and collected in reflective configuration with an Andor spectrometer with EMCCD iXon Ultra.

## Supporting Information

Supporting Information is available from the Wiley Online Library or from the author.

## Acknowledgements

The authors acknowledge the provision of facilities and technical support by Aalto University at OtaNano - Nanomicroscopy Center (Aalto-NMC). The authors acknowledge funding from the Research Council of Finland (314810, 333982, 336144, 349971, 352780, 352930, and 353364), the Research Council of Finland Flagship Programme (320167, PREIN), the EU H2020-MSCA-RISE-872049 (IPN-Bio), the Jane and Aatos Erkko foundation and the Technology Industries of Finland centennial foundation (Future Makers 2022), and ERC (834742; 101082183). Aalto Science-IT is acknowledged for computational resources. The authors would like to thank Dr. Shang Nianze for his guidance with wavelength-dependent THG measurements.

## Conflict of Interest

The authors declare no conflict of interest

## Data Availability Statement

The data that support the findings of this study are available from the corresponding author upon reasonable request.

## Keywords

defect engineering, femtosecond laser, nonlinear optics, optical modification, second harmonic generation, transition metal dichalcogenides

Received: April 23, 2024
Revised: August 23, 2024
Published online:

[1] K. S. Novoselov, A. Mishchenko, A. Carvalho, A. H. C. Neto, *Science* **2016**, *353*, 1.
[2] A. C. Ferrari, F. Bonaccorso, V. Fal'ko, K. S. Novoselov, S. Roche, P. Bøggild, S. Borini, F. H. Koppens, V. Palermo, N. Pugno, J. A. Garrido, R. Sordan, A. Bianco, L. Ballerini, M. Prato, E. Lidorikis, J. Kivioja, C. Marinelli, T. Ryhänen, A. Morpurgo, J. N. Coleman, V. Nicolosi, L. Colombo, A. Fert, M. Garcia-Hernandez, A. Bachtold, G. F. Schneider, F. Guinea, C. Dekker, M. Barbone, et al., *Nanoscale* **2015**, *7*, 4598.
[3] S. Manzeli, D. Ovchinnikov, D. Pasquier, O. V. Yazyev, A. Kis, *Nat. Rev. Mater.* **2017**, *2*, 17033.
[4] R. J. Toh, Z. Sofer, J. Luxa, D. Sedmidubský, M. Pumera, *Chem. Commun.* **2017**, *53*, 3054.
[5] A. Autere, H. Jussila, Y. Dai, Y. Wang, H. Lipsanen, Z. Sun, *Adv. Mater.* **2018**, *30*, 1.
[6] A. A. Tedstone, D. J. Lewis, P. O'Brien, *Chem. Mater.* **2016**, *28*, 1965.
[7] E. Kim, C. Ko, K. Kim, Y. Chen, J. Suh, S.-G. Ryu, K. Wu, X. Meng, A. Suslu, S. Tongay, J. Wu, C. P. Grigoropoulos, *Adv. Mater.* **2016**, *28*, 341.
[8] H. G. Rosa, L. Junpeng, L. C. Gomes, M. J. L. F. Rodrigues, S. C. Haur, J. C. V. Gomes, H. G. Rosa, L. Junpeng, L. C. Gomes, M. J. L. F. Rodrigues, S. C. Haur, J. C. V. Gomes, *Adv. Opt. Mater.* **2018**, *6*, 1701327.
[9] F. Liu, Z. Fan, *Chem. Soc. Rev.* **2023**, *52*, 1723.
[10] D. Rhodes, D. A. Chenet, B. E. Janicek, C. Nyby, Y. Lin, W. Jin, D. Edelberg, E. Mannebach, N. Finney, A. Antony, T. Schiros, T. Klarr, A. Mazzoni, M. Chin, Y. C. Chiu, W. Zheng, Q. R. Zhang, F. Ernst, J. I. Dadap, X. Tong, J. Ma, R. Lou, S. Wang, T. Qian, H. Ding, R. M. Osgood, D. W. Paley, A. M. Lindenberg, P. Y. Huang, A. N. Pasupathy, et al., *Nano Lett.* **2017**, *17*, 1616.
[11] M. Turunen, M. Brotons-Gisbert, Y. Dai, Y. Wang, E. Scerri, C. Bonato, K. D. Jöns, Z. Sun, B. D. Gerardot, *Nat. Rev.* **2022**, *4*, 219.
[12] Q. Zhang, A. T. Wee, Q. Liang, X. Zhao, M. Liu, *ACS Nano* **2021**, *15*, 2165.
[13] S. M. Akkanen, H. A. Fernandez, Z. Sun, *Adv. Mater.* **2022**, *34*, 19.
[14] P. Koskinen, K. Karppinen, P. Myllyperkiö, V. M. Hiltunen, A. Johansson, M. Pettersson, *J. Phys. Chem. Lett.* **2018**, *9*, 6179.
[15] T. Kähärä, P. Koskinen, *Phys. Rev. B* **2020**, *102*, 75433.
[16] A. Johansson, P. Myllyperkiö, P. Koskinen, J. Aumanen, J. Koivistoinen, H. C. Tsai, C. H. Chen, L. Y. Chang, V. M. Hiltunen, J. J. Manninen, W. Y. Woon, M. Pettersson, *Nano Lett.* **2017**, *17*, 6469.
[17] V. M. Hiltunen, P. Koskinen, K. K. Mentel, J. Manninen, P. Myllyperkiö, A. Johansson, M. Pettersson, *J. Phys. Chem. C* **2020**, *124*, 8371.
[18] V. M. Hiltunen, P. Koskinen, K. K. Mentel, J. Manninen, P. Myllyperkiö, M. Pettersson, A. Johansson, *npj 2D Mater. Appl.* **2021**, *5*, 1.
[19] M. T. Turunen, E. Hulkko, K. K. Mentel, X. Bai, S.-T. Akkanen, M. Amini, S. Li, H. Lipsanen, M. Pettersson, Z. Sun, *Adv. Mater. Interfaces* **2021**, *8*, 2002119.
[20] H. Lin, Z. Q. Xu, G. Cao, Y. Zhang, J. Zhou, Z. Wang, Z. Wan, Z. Liu, K. P. Loh, C. W. Qiu, Q. Bao, B. Jia, *Light: Sci. Appl.* **2020**, *9*, 1.
[21] X. Liu, M. C. Hersam, *Nat. Rev. Mater.* **2019**, *4*, 669.
[22] Y. Chen, S. Huang, X. Ji, K. Adepalli, K. Yin, X. Ling, X. Wang, J. Xue, M. Dresselhaus, J. Kong, B. Yildiz, *ACS Nano* **2018**, *12*, 2569.
[23] P. L. McMahon, *Nat. Rev. Phys.* **2023**, *5*, 717.
[24] L. Hou, H. Li, Q. Wang, X. Gan, F. Xiao, J. Zhao, *Nanophotonics* **2024**, *13*, 349.
[25] Z. Zhang, L. Zhang, R. Gogna, Z. Chen, H. Deng, *Solid State Commun.* **2020**, *322*, 114043.
[26] D. Li, C. Wei, J. Song, X. Huang, F. Wang, K. Liu, W. Xiong, X. Hong, B. Cui, A. Feng, L. Jiang, Y. Lu, *Nano Lett.* **2019**, *19*, 4195.
[27] H. Hong, C. Wu, Z. Zhao, Y. Zuo, J. Wang, C. Liu, J. Zhang, F. Wang, J. Feng, H. Shen, J. Yin, Y. Wu, Y. Zhao, K. Liu, P. Gao, S. Meng, S. Wu, Z. Sun, K. Liu, J. Xiong, *Nat. Photonics* **2021**, *15*, 510.
[28] Z. Zhou, H. Xu, Y. Yu, L. Lin, X. Wang, *Laser Photonics Rev.* **2021**, *15*.
[29] J. Zhao, H. Lu, J. Zheng, D. Li, Y. Zhang, X. Gan, J. Zhao, *Opt. Lett.* **2024**, *49*, 3130.
[30] R. W. Boyd, A. L. Gaeta, E. Giese, *Nonlinear Optics*, Springer, New York **2008**.
[31] K. K. Mentel, J. Manninen, V.-M. Hiltunen, P. Myllyperkiö, A. Johansson, M. Pettersson, *Nanoscale Adv.* **2021**, *3*, 1431.
[32] Y. Liu, H. Nan, X. Wu, W. Pan, W. Wang, J. Bai, W. Zhao, L. Sun, X. Wang, Z. Ni, *ACS Nano* **2013**, *7*, 4202.
[33] A. Jain, P. Bharadwaj, S. Heeg, M. Parzefall, T. Taniguchi, K. Watanabe, L. Novotny, *Nanotechnology* **2018**, *29*, 265203.
[34] J. Jung, H. Bark, D. Byun, C. Lee, D. H. Cho, *2D Mater.* **2019**, *6*, 025024.
[35] X.-J. Zhang, *Van der Waals Forces*, Springer, Boston, MA **2013**.
[36] Z. Lin, B. R. Carvalho, E. Kahn, R. Lv, R. Rao, H. Terrones, M. A. Pimenta, M. Terrones, *2D Mater.* **2016**, *3*, 022002.
[37] H. Liu, D. Chi, *Sci. Rep.* **2015**, *5*, 11756.
[38] W. M. Parkin, A. Balan, L. Liang, P. M. Das, M. Lamparski, C. H. Naylor, J. A. Rodríguez-Manzo, A. T. Johnson, V. Meunier, M. Drndić, *ACS Nano* **2016**, *10*, 4134.

[39] M. W. Iqbal, K. Shahzad, R. Akbar, G. Hussain, *Microelectron. Eng.* **2020**, *219*, 111152.
[40] N. M. Badlyan, N. Pettinger, N. Enderlein, R. Gillen, X. Chen, W. Zhang, K. C. Knirsch, A. Hirsch, J. Maultzsch, *Phys. Rev. B* **2022**, *106*, 104103.
[41] Z. Liu, H. Cai, F. Wang, Z. Quan, T. Xiong, M. Tian, Q. Lu, C. Ye, C. Zhang, J. Tan, *Adv. Energy Mater.* **2024**, *14*, 2400470.
[42] A. Castellanos-Gomez, R. Roldán, E. Cappelluti, M. Buscema, F. Guinea, H. S. V. D. Zant, G. A. Steele, *Nano Lett.* **2013**, *13*, 5361.
[43] P. Zuo, L. Jiang, X. Li, P. Ran, B. Li, A. Song, M. Tian, T. Ma, B. Guo, L. Qu, Y. Lu, *Nanoscale* **2019**, *11*, 485.
[44] S. Tongay, J. Suh, C. Ataca, W. Fan, A. Luce, J. S. Kang, J. Liu, C. Ko, R. Raghunathanan, J. Zhou, F. Ogletree, J. Li, J. C. Grossman, J. Wu, *Sci. Rep.* **2013**, *3*, 1.
[45] S. Bertolazzi, S. Bonacchi, G. Nan, A. Pershin, D. Beljonne, P. Samorí, *Adv. Mater.* **2017**, *29*, 1606760.
[46] T. Korn, S. Heydrich, M. Hirmer, J. Schmutzler, C. Schüller, *Appl. Phys. Lett.* **2011**, *99*, 102109.
[47] Z. He, R. Zhao, X. Chen, H. Chen, Y. Zhu, H. Su, S. Huang, J. Xue, J. Dai, S. Cheng, M. Liu, X. Wang, Y. Chen, *ACS Appl. Mat. Interfaces* **2018**, *10*, 42524.
[48] L. Mennel, M. M. Furchi, S. Wachter, M. Paur, D. K. Polyushkin, T. Mueller, *Nat. Commun.* **2018**, *9*, 1.
[49] L. Mennel, M. Paur, T. Mueller, *APL Photonics* **2018**, *4*, 034404.
[50] S. Mignuzzi, A. J. Pollard, N. Bonini, B. Brennan, I. S. Gilmore, M. A. Pimenta, D. Richards, D. Roy, *Phys. Rev. B* **2015**, *91*, 195411.
[51] C. Janisch, Y. Wang, D. Ma, N. Mehta, A. L. Elías, N. Perea-López, M. Terrones, V. Crespi, Z. Liu, *Sci. Rep.* **2014**, *4*, 1.
[52] I. H. Malitson, *J. Opt. Soc. Am.* **1965**, *55*, 1205.
[53] A. Säynätjoki, L. Karvonen, H. Rostami, A. Autere, S. Mehravar, A. Lombardo, R. A. Norwood, T. Hasan, N. Peyghambarian, H. Lipsanen, K. Kieu, A. C. Ferrari, M. Polini, Z. Sun, *Nat. Commun.* **2017**, *8*, 1.
[54] H. Liu, J. Lu, K. Ho, Z. Hu, Z. Dang, A. Carvalho, H. R. Tan, E. S. Tok, C. H. Sow, *Nano Lett.* **2016**, *16*, 5559.
[55] W. Murray, M. Lucking, E. Kahn, T. Zhang, K. Fujisawa, N. Perea-Lopez, A. L. Elias, H. Terrones, M. Terrones, Z. Liu, *2D Mater.* **2020**, *7*, 045020.
[56] A. W. Murphy, Z. Liu, A. V. Gorbach, A. Ilie, V. K. Valev, *Laser Photonics Rev.* **2021**, *15*, 2100117.
[57] P. Li, X. Jiang, M. Huang, L. Kang, S. Chen, A. Gali, B. Huang, *Cell Rep. Phys. Sci.* **2022**, *3*, 101111.
[58] T. Y. Ko, A. Jeong, W. Kim, J. Lee, Y. Kim, J. E. Lee, G. H. Ryu, K. Park, D. Kim, Z. Lee, M. H. Lee, C. Lee, S. Ryu, *2D Mater.* **2016**, *4*, 014003.
[59] N. D. Baydoğan, *Mater. Sci. Eng., B* **2004**, *107*, 70.
[60] Y. Wang, S. Das, X. Hu, Y. Dai, X. Bai, Z. Sun, in *Conf. on Lasers and Electro-Optics (CLEO)*, Optica Publishing Group, Washington, DC **2020**, pp. 1–2.
[61] N. Mendelson, D. Chugh, J. R. Reimers, T. S. Cheng, A. Gottscholl, H. Long, C. J. Mellor, A. Zettl, V. Dyakonov, P. H. Beton, S. V. Novikov, C. Jagadish, H. H. Tan, M. J. Ford, M. Toth, C. Bradac, I. Aharonovich, *Nat. Mater.* **2021**, *20*, 321.
[62] R. A. John, J. Acharya, C. Zhu, A. Surendran, S. K. Bose, A. Chaturvedi, N. Tiwari, Y. Gao, Y. He, K. K. Zhang, M. Xu, W. L. Leong, Z. Liu, A. Basu, N. Mathews, *Nat. Commun.* **2020**, *11*, 1.
[63] J. B. Roldan, D. Maldonado, C. Aguilera-Pedregosa, E. Moreno, F. Aguirre, R. Romero-Zaliz, A. M. García-Vico, Y. Shen, M. Lanza, *npj 2D Mater. Appl.* **2022**, *6*, 1.
[64] X. Zhao, H. Zhu, X. Yang, *Nanoscale* **2014**, *6*, 10680.
[65] H. Deng, C. Zhang, Y. Xie, T. Tumlin, L. Giri, S. P. Karna, J. Lin, *J. Mater. Chem. A* **2016**, *4*, 6824.
[66] H. Su, X. Pan, S. Li, H. Zhang, R. Zou, *Carbon Energy* **2023**, *5*, e296.
[67] K. K. Mentel, A. V. Emelianov, A. Philip, A. Johansson, M. Karppinen, M. Pettersson, K. K. Mentel, A. V. Emelianov, A. Johansson, M. Pettersson, A. Philip, M. Karppinen, *Adv. Mater. Interfaces* **2022**, *9*, 2201110.
[68] S. Shree, D. Lagarde, L. Lombez, C. Robert, A. Balocchi, K. Watanabe, T. Taniguchi, X. Marie, I. C. Gerber, M. M. Glazov, L. E. Golub, B. Urbaszek, I. Paradisanos, *Nat. Commun.* **2021**, *12*, 1.